Optics Communications 313 (2014) 186–194

Contents lists available at ScienceDirect

Optics Communications

journal homepage: www.elsevier.com/locate/optcom

Silicon-on-sapphire waveguides design for mid-IR evanescent field absorption gas sensors

Yuewang Huang [a,*], Salih K. Kalyoncu [a], Qiancheng Zhao [a], Rasul Torun [a], Ozdal Boyraz [a,b]

[a] Department of EECS, University of California, 5019 Engineering Hall, Irvine, CA 92697-2625, USA
[b] Department of EEE, Istanbul Sehir University, Istanbul, Turkey

ARTICLE INFO

Article history:
Received 26 July 2013
Received in revised form
6 September 2013
Accepted 5 October 2013
Available online 19 October 2013

Keywords:
Silicon-on-sapphire waveguide
Evanescent field absorption
Evanescent gas sensors
Mid infrared
Waveguide propagation loss

ABSTRACT

Major trace gases have absorption lines in mid-IR. We propose silicon-on-sapphire waveguides at mid-IR for gas sensing based on evanescent field absorption. This can provide a general platform for multipurpose sensing of different types of gases in a reusable fashion. Three types of waveguides (strip, rib and slot) are investigated on their geometrical dependence of evanescent-field ratio (EFR) and propagation loss to serve as the proposed gas sensor. Slot waveguide provides the highest EFR ($>25\%$) in mid-IR with moderate dimension, but its fabrication can be more challenging and its high loss (~ 10 dB/cm) impairs the sensing resolution and necessitates higher input power in longer waveguides. Strip and rib waveguides can achieve similar EFR with smaller dimensions. We analyze the detection of CO_2 in atmosphere based on its mid-IR absorption peak at ~ 4.23 μm as a case study. Numerical analysis based on up-to-date commercial mid-IR detector parameters shows that a resolution of 2 ppm, 5 ppm and 50 ppm can be achieved in cooled InSb, room-temperature HgCdTe and room-temperature PbSe detectors respectively by using 1 cm waveguides. Effect of waveguide loss also has been investigated.

1. Introduction

Gas sensors have found wide applications and high demands in chemistry, biology, medicine, manufacturing and environmental industry [1]. Major types of gas sensors include catalytic, electrochemical, thermal, ultrasonic, semiconductor and infrared sensors. Their detection mechanisms can rely on the thermal, chemical, mechanical, electrical or optical property of the functional material [2]. However, most of these sensors are bulky and some even require a thermal management system [2]. Their integrability and portability are limited and they are not applicable in scenarios where limited space is available. It is attractive to have miniature sensors that could be fitted into small chip areas. In this way, they could be integrated with on-chip control and processing circuits to build a chip-scale sensing system, which can be deployed in distributed sensing networks. Chip-level gas sensors have been demonstrated using micro-ring resonators and Mach–Zehnder interferometers in near-IR spectrum [3,4]. They both utilize the refractive index variation due to different types and concentrations of the gas immersing the evanescent field. However, the refractive index change by the gas itself alone in these sensors is too small to be detected. A film is often required to be coated on device surfaces to enhance the refractive index variation and hence to increase the sensitivity. However, a particular film is often reactive to only one type of gas and different materials have to be deposited for different gas species. Hence, a general-purpose sensor is not applicable. Moreover, the response time is also limited by the chemical or physical reaction rate and its lifetime is usually short. To probe further, besides refractive index change, gas type and concentration also affect the absorption experienced by the evanescent field. This property in planar waveguides can be also utilized to achieve gas sensing as has been shown in fiber optics [5–7]. While fiber optics and waveguide technology are well-developed and become mature in the famous near-IR telecommunication band, there are very few types of industrially or environmentally important gases with absorption peaks in the near-IR wavelengths. In contrast, the mid-IR spectrum window contains absorption peaks for a wide variety of trace gases, including H_2O, CO, CO_2, NO, N_2O, NO_2 and CH_4 [5,8]. If viable waveguide-based sensors for these gases are available at affordable price, they can be integrated with electrical circuitry to support system-on-chip applications for chemical, biological, industrial and environmental monitoring. Unfortunately, the SOI and fiber technology cannot be extended easily to mid-IR due to the strong loss associated with the oxide layer. Free-standing silicon waveguides with air substrate are proposed to circumvent this limitation in mid-IR [8–10]. However, this type of waveguide is unstable mechanically or optically in the long term especially under harsh natural conditions, where the sensors usually are. Another way to circumvent the substrate loss is to use a non-lossy substrate material. Among many proposed candidates, sapphire has gained popularity for its superior mechanical and thermal stability and a transparency window up to ~ 6 μm. Silicon-on-sapphire (SOS) waveguides are proposed and proven to be a good mid-IR

* Corresponding author. Tel.: +1 9497 328 317.
E-mail addresses: yuewangh@uci.edu, yuewangh@gmail.com (Y. Huang).

0030-4018/$ - see front matter © 2013 Elsevier B.V. All rights reserved.
http://dx.doi.org/10.1016/j.optcom.2013.10.022

alternative to SOI in the near-IR [11–16]. With the abundance of gas absorption peaks in the mid-IR spectra, SOS platform can support the detection of all the gas species mentioned earlier.

In this paper, we propose an evanescent field absorption gas sensor based on SOS waveguide in mid-IR wavelength. This provides a general solution to the sensing of different trace gases, which could result in inexpensive and robust miniature gas sensors with fast response and large reusability. Another advantage is that the platform can potentially be used to detect different types of gases at the same time with broadband mid-IR sources (e.g. thermal radiators). The mid-IR optical signal can be detected indirectly using silicon waveguide and near-IR detectors [16,17]. Meanwhile, mid-IR sources are getting available also through the parametric process in silicon waveguides [18,19]. Also integrated mid-IR detectors on a silicon substrate have been also demonstrated [20,21]. With further advancements in mid-IR photonics, an on-chip gas sensing system would become possible in the foreseeable future. The paper is organized mainly in three parts. We first present the sensing mechanism of the proposed SOS waveguide based absorption evanescent sensor. The SOS waveguide is then designed for high detection resolution of the target gas concentration. Evanescent field ratio (EFR) is defined as the ratio of evanescent field power in the cladding to the total power of the waveguide mode. The geometrical dependence of EPR, as well as propagation loss, provides a guideline for the design of SOS waveguide for mid-IR absorption sensing application. In particular, three types of common waveguides (strip, rib and slot waveguides) are included in the design. Although all three types are capable of delivering a platform to sense the target gas with high resolution, slot waveguide is shown to possess the highest EFR values with moderate dimension and hence higher sensing performance if other conditions are the same. However, it is more fabrication intensive and prone to having higher propagation loss, which makes a higher input power necessary to compensate the loss and to maintain acceptable sensing resolution for longer waveguides. On the other hand, rib waveguide offers the lowest propagation loss among the three types, favoring its application as an evanescent gas sensor. In the end, we apply this sensing mechanism to detect CO_2 concentration fluctuation at the atmospheric base level. Our analysis based on the up-to-date mid-IR detector parameters shows that a resolution as low as 2 ppm can be readily achieved with these waveguides at atmospheric environment.

2. Evanescent absorption sensing

As light travels through the silicon waveguide, most of the energy is confined within the silicon core. However, as shown in Fig. 1, there will be also evanescent field extending to the substrate region and cladding region formed by the surrounding media. In the cladding, the wave interacts with the gas surrounding the waveguide and goes through power attenuation if the light wavelength is properly aligned with the absorption lines of the gas. The absorption is dependent on the concentration of the target gas. The power transmitted through the waveguide can be characterized using the Beer–Lambert law as follows [5]:

$$I(c) = I_0 \exp(-\eta \varepsilon c l - \alpha_0 l) \tag{1}$$

I_0 is the input power to the waveguide; ε and c are the absorption coefficient and concentration of the target gas, respectively. l is the length of the waveguide and α_0 is the intrinsic loss of the waveguide, including the linear loss and coupling loss distributed along the waveguide length. It is noteworthy that the gas absorption will result in excess loss on top of static loss of the system and it is this incremental loss that is critical for the sensing. The influence of variation on the coupling loss can be minor because the system can be sealed mechanically. We will analyze the influence of different static propagation losses on the sensing performance in the forthcoming sections. η is the evanescent field ratio (EFR), which is defined as the ratio of evanescent field power in the cladding gas to the total modal power:

$$\eta = \iint_{Gas} \vec{S} \bullet \vec{n}\, dx\, dy \div \iint_{All} \vec{S} \bullet \vec{n}\, dx\, dy \tag{2}$$

where $\vec{S}$ is the Poynting Vector of the mode field in the waveguide and $\vec{n}$ is the normal vector to the waveguide cross-section. By differentiating Eq. (1) with respect to the concentration c, we get the sensor's sensitivity to the change of the gas concentration as follows:

$$S = \frac{dI}{dc} = -\eta \varepsilon l I_0 \exp(-\eta \varepsilon c l - \alpha_0 l) \tag{3}$$

The light at the output is detected with mid-IR detectors. Commercial mid-IR detectors include photoconductive, photovoltaic and thermal detectors. Since thermal detectors are too slow and suffer from thermal drifting issue, only photoconductive (PC) and photovoltaic (PV) detectors are analyzed here. Photovoltaic detectors absorb photons with energy beyond and near their band-gap to generate current. Because the energy associated with mid-IR photons corresponds to a narrow band-gap, thermal generation can result in considerable dark current. Low temperature operation is always necessary to suppress dark current and the shot noise associated with it. The noise components in photovoltaic detectors include thermal noise, shot noise and flicker noise. If a low-pass filter is inserted to eliminate flicker noise, the total noise $i^2_{n,pv}$ will mainly consist of thermal noise $i^2_{n,th}$ and shot noise $i^2_{n,sh}$ as follows:

$$i^2_{n,th} = 4(k_b T / R_L) F_n B_e \tag{4}$$

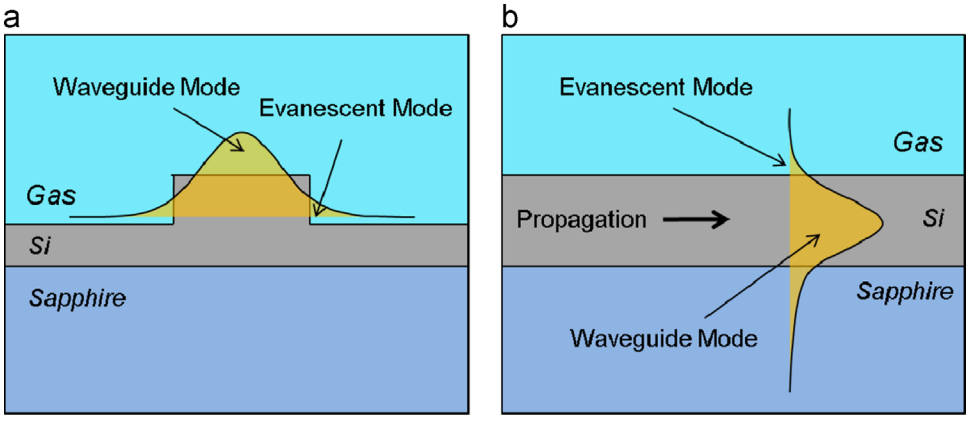

Fig. 1. Schematics of the evanescent absorption gas sensor: (a) cross-sectional view and (b) side view.

$$i_{n,sh}^2 = 2q[RI(c)+i_d]B_e \tag{5}$$

where R_L is load resistance, F_n is the circuitry noise figure, R is the responsivity of the detector, B_e is the electrical bandwidth, and $I(c)$ is the incident power to the mid-IR detector [22]. In the photoconductive mode, photo-generated carriers change the conductivity of the medium and lead to a change in the voltage across the medium. Due to different detection mechanisms, the noise composition in photoconductive detectors is also different from photovoltaic ones. Main noise components in photoconductive detectors include thermal noise, generation–recombination noise (GR-noise), background noise, flicker noise and also the noise transferred from voltage supply. While supply voltage induced noise can be minimized to negligible level by using low noise voltage supplies and flicker noise also can be eliminated by low-pass filters, the total noise $i_{n,pc}^2$ mainly includes thermal noise $i_{n,th}^2$, GR-noise $i_{n,gr}^2$ and background noise $i_{n,bg}^2$ [23,24]:

$$i_{n,gr}^2 = \int_0^{B_e} \frac{4qi_0\Gamma_G}{(1+4\pi^2f^2\tau^2)}df = \frac{2qi_0\Gamma_G}{\pi\tau}\tan^{-1}(2\pi B_e\tau) \tag{6}$$

$$i_{n,bg}^2 = q^2\phi AE_{BB}B_e \tag{7}$$

where τ is average carrier lifetime, i_0 is the total generation current, Γ_G is the current gain, ϕ is quantum efficiency, A is active detector area, $E_{BB} = \int_0^{\lambda_c} \varepsilon_\lambda \frac{2\pi c}{\lambda^4}\left[\frac{1}{e^{hc/\lambda k_b T}-1}\right]d\lambda$ is the total photon flux density with λ_c being the cut-off wavelength and ε_λ the emissivity for the window material.

There is also noise associated with the intensity fluctuation of the light source. This intensity noise will be also attenuated by the waveguide and can be referred to the input of the detector as optical noise power [24]:

$$I_{RIN}^2 = \mathrm{RIN}\, I_0^2 B_e \exp(-2\eta\varepsilon cl - 2\alpha_0 l) \tag{8}$$

where RIN is the relative intensity noise of the laser. The detector noises $i_{n,pv}^2$ and $i_{n,pc}^2$ can be also referred to optical power at the detector input as follows:

$$I_{n,pv}^2 = \frac{i_{n,pv}^2}{R^2} = \frac{i_{n,th}^2+i_{n,sh}^2}{R^2} \tag{9}$$

$$I_{n,pc}^2 = \frac{i_{n,pc}^2R_L^2}{R^2} = \frac{(i_{n,th}^2+i_{n,gr}^2+i_{n,bg}^2)R_L^2}{R^2} \tag{10}$$

The total intensity-referred noise will determine the limit of detectable optical power level. Combining with the sensitivity in Eq. (3), we can derive the resolution of the gas sensor Δc, defined as the minimum resolvable gas concentration fluctuation for a signal-to-noise ratio greater than unity, using PV or PC detectors as follows:

$$\Delta c = \begin{cases} \frac{\sqrt{I_{n,pv}^2+I_{RIN}^2}}{|S|}, & PV \\ \frac{\sqrt{I_{n,pc}^2+I_{RIN}^2}}{|S|}, & PC \end{cases} \tag{11}$$

3. Waveguide design

According to Eq. (3), in order to increase the detection sensitivity, the waveguides need to be designed for maximum gas–field interaction to achieve a large η value. A waveguide with small electrical dimension is generally desired to support strong evanescent field [25]. In this paper, we investigate three types of SOS waveguides, including strip, rib and slot waveguides, for absorption based gas sensing in mid-IR as shown in Fig. 2. W and H are the width and height of waveguide, respectively. T is the thickness of the dielectric slab layer in rib waveguide and S is the width of the slot in slot waveguide. As an example, we design the waveguide for the wavelength of 4.23 μm, which corresponds to an absorption line of CO_2 in mid-IR. The simulated η values will be used in the case study of CO_2 sensing in the next section.

In strip waveguide, both quasi-TE and quasi-TM modes are of interest for field enhancement, because the gas will be interacting with the evanescent field on the top and at the two sidewalls of the waveguide. For quasi-TE mode, the dominant electrical field is in the horizontal direction, which will be enhanced at the gas interface with the sidewalls to satisfy the electrical displacement continuity condition, $\varepsilon_{Si}E_{Si} = \varepsilon_{Gas}E_{Gas}$. The electrical field jumps up due to lower dielectric constant in the gas compared to silicon core as shown in Fig. 3(b) and (c). In this case, the electrical field is almost as strong as in the waveguide core. As the waveguide gets narrower, the mode gets squeezed and the evanescent field can jump to a even higher level and hence produces pronounced enhancement. This, in turn, leads to an increase in the EFR as shown in Fig. 3(a). However, there is a limit on the benefit we can gain out of narrowing the waveguide. When W gets too small ($W < 0.8$ μm in this case), the quasi-TE mode gets leaky and it is no longer supported as a guiding mode. EFR saturates for large W values because the energy will mostly be confined laterally in the silicon core and most of the evanescent field will be from the top–wall interface. In the vertical direction, however, EFR depends less heavily on the waveguide height H. This is because the tangential electrical field in this case is continuous and no enhancement can be expected from the dielectric constant discontinuity. Nevertheless, EFR still becomes larger as we shrink H, especially when H is small. In the quasi-TM mode, vertical electrical field is dominant. And for the same reason as in the quasi-TE mode, the evanescent field will be enhanced at the top cladding as shown in Fig. 4(b) and (c). The EFR is sensitive to waveguide height and it depends on H in a similar fashion as it does on W in the quasi-TE mode, Fig. 4(c). Meanwhile, greater waveguide width still reduces the EFR. Leaky mode will also come into play when W and H become too small.

Rib waveguide provides more design freedom by inserting a silicon slab layer to aid wave guiding. Achievable EFR can exceed that in strip waveguide, because modes can remain guided for smaller dimensions. At the same time, the bell shape mode profile also leads to more evanescent field distribution in the cladding region near the two shoulder corners where the gas resides. Since the quasi-TE mode in rib waveguide has considerable portion of field distributed in the two shoulders of the rib [26], the EFR is

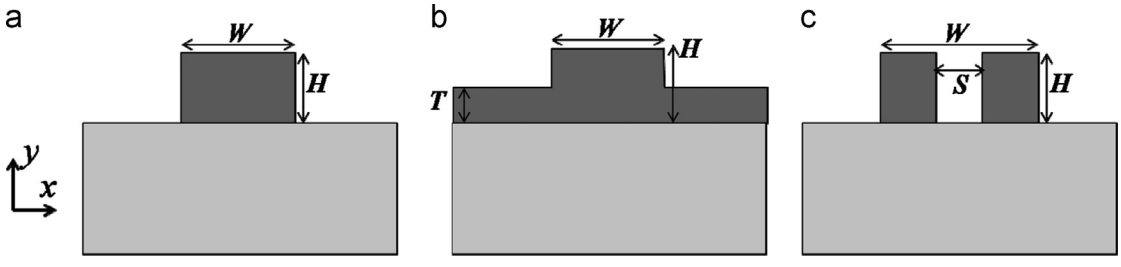

Fig. 2. Three main types of waveguides investigated: (a) strip, (b) rib and (c) slot waveguides.

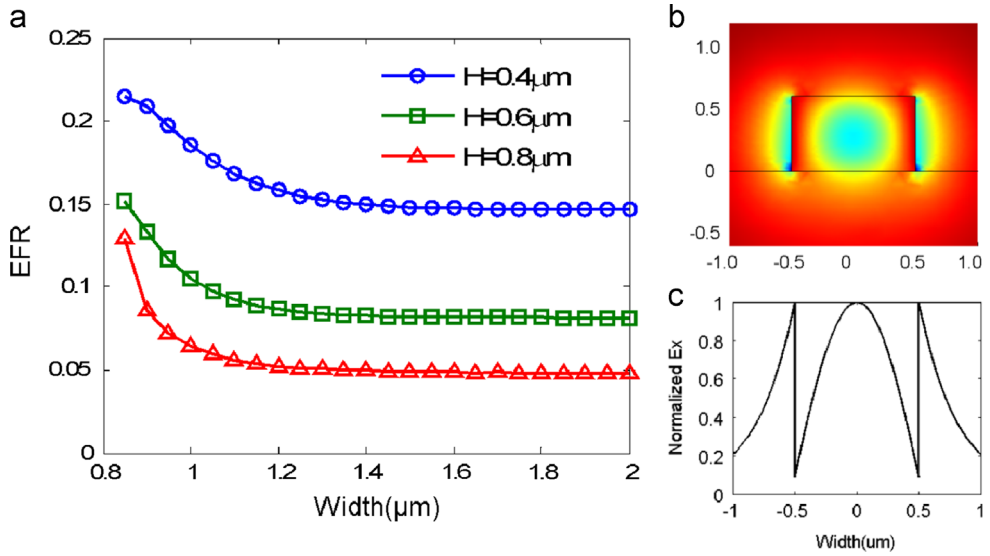

Fig. 3. Quasi-TE mode in strip waveguide: (a) EFR versus waveguide width, (b) mode distribution at 4.23 μm ($W=1$ μm, $H=0.6$ μm), and (c) normalized E_x field along X direction.

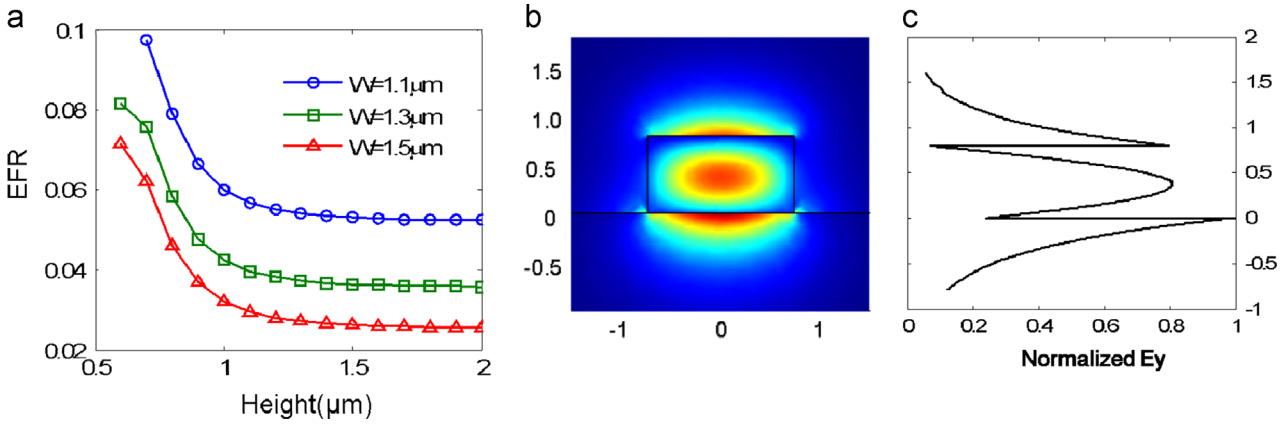

Fig. 4. Quasi-TM mode in strip waveguide: (a) EFR versus waveguide height, (b) mode distribution at 4.23 μm ($W=1.3$ μm, $H=1$ μm), and (c) normalized E_y field along Y direction.

sensitive to slab thickness T as shown in Fig. 5. When W is small, larger T tends to give smaller EFR. Interestingly, this tendency is gently reversed when the ridge gets wider. To understand this by examining the mode profiles, when W is small, there is considerable field distribution in the corner between the ridge shoulder and the slab and the increasing of H will push the gas out of this region. This results in a drop in the EFR values. When W is relatively large, this contribution is diminished due to weak field distribution in the corner. However, thickening the slab will shift the overall mode up slightly and hence increase the EFR contribution from the top waveguide wall. EFR lessens as W or H increases due to better confinement in the waveguide core in both cases. Quasi-TM mode in rib waveguide has most of its energy concentrated in the center ridge and EFR is hence insensitive to slab height T as shown in Fig. 6. And higher H degrades EFR, but less prominently as H gets larger for the same reason as stated before.

Slot waveguide is widely investigated in evanescent field based applications, since it typically provides good field–matter interaction in the slot [3]. For the slot waveguide shown in Fig. 2(c), only quasi-TE is investigated because evanescent field in the slot is enhanced in this mode. As shown in Fig. 7, slot width plays an important role in determining EFR. When the S/W ratio is high, mode distribution will be squeezed into the slot region and EFR is dominated by the field enhancement in the slot. Although the slot area would get smaller as S decreases, the evanescent field enhancement in the slot overtakes the slot area decrease and maximum achievable EFR could still improve from 22% for $S=0.4$ μm to 27% for $S=0.2$ μm. Meanwhile, the optimal W for maximum EFR also increases proportionally with S. With moderate S/W ratio, the area of slot is critical and greater S provides slightly higher EFR. When S/W ratio is small, however, the mode will be mostly concentrated in silicon grooves and the EFR values are insensitive to the slot width. In the vertical dimension, decreased H will help to boost EFR due to stronger evanescent field in the cladding.

It is clear from Section 2 that, besides the evanescent-field ratio, loss in the system also plays a critical role in sensor performance. For instance, the coupling loss is important in determining the coupling intensity. However, the analysis of coupling loss is subject to the choice of coupling methods and light sources; hence instead of providing a detailed and lengthy analysis we assume a pessimistic estimation of −15 dB coupling loss in the next section. Meanwhile, we also want to point out that the static coupling loss can always be compensated by increasing the input power. Alternatively, the waveguide propagation loss, mainly including scattering loss and substrate leakage, is strongly

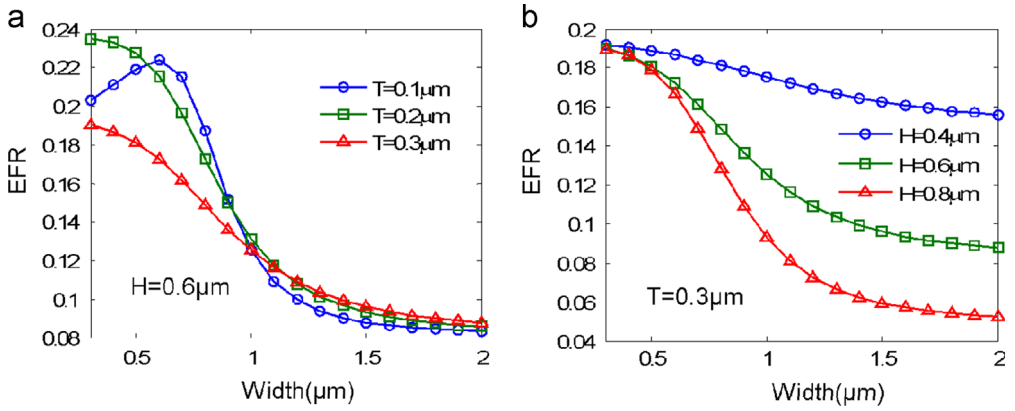

Fig. 5. EFR versus waveguide width for the quasi-TE mode in rib waveguide: (a) grouped with different slab thicknesses and (b) grouped with different waveguide heights.

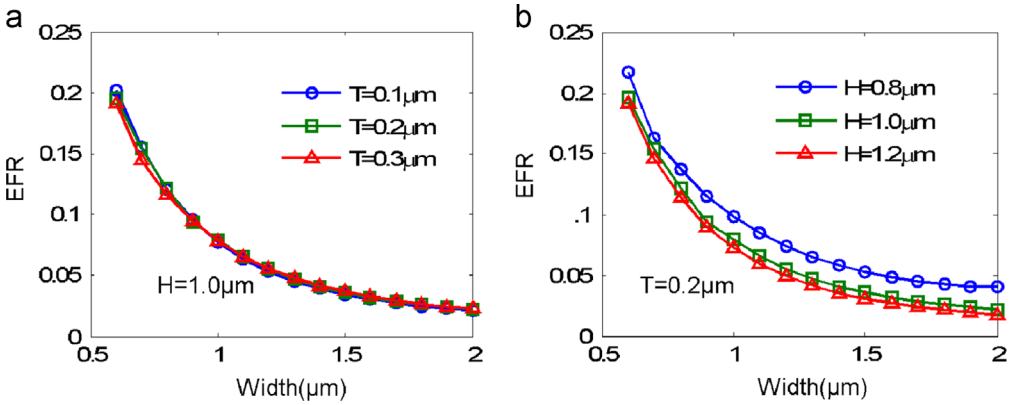

Fig. 6. EFR versus waveguide width for the quasi-TM mode in rib waveguide: (a) grouped with different slab thicknesses and (b) grouped with different waveguide heights.

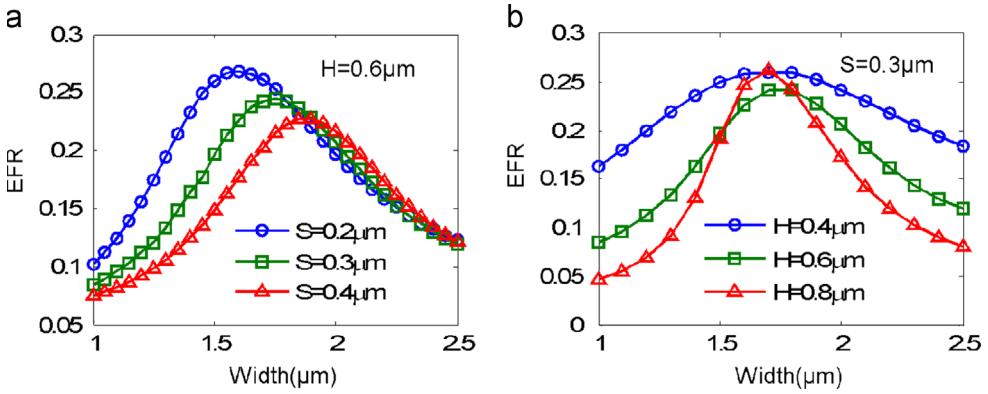

Fig. 7. EFR versus waveguide width for the quasi-TE mode in slot waveguide: (a) grouped with different slot spacings and (b) grouped with different waveguide heights.

dependent on the waveguide geometries. In this section, we will investigate propagation loss for different waveguide types and geometries. There has been extensive study on the modeling of waveguide scattering loss, notably 2D volume–current method (VCM) [27], 3D VCM [28,29] and 3D coupled-mode method [30]. While the 2D VCMs are simple, they are limited to simple waveguide geometries in homogeneous medium and the loss can be substantially overestimated [29]. Here we employed the 3D VCM proposed in [29] due to its high accuracy and applicability to complex waveguide geometries. In this method, the scattering from the rough sidewalls is modeled as an effective volume current density expressed as follows [29]:

$$\vec{J} = -i\omega\varepsilon_0(n_1^2 - n_2^2)\vec{E}(0,y)\delta(x)\delta(z) \tag{12}$$

$\vec{E}(0,y)$ is electrical field along the sidewall calculated from an FEM mode solver [31]. n_1 and n_2 are refractive indices inside and outside the waveguide core, respectively. We then calculate the far-field radiation with this elementary current density in the same dielectric waveguide using a 3D FEM solver [31]. The scattering loss α_{sc} is then derived by integrating the far-field power density flow on a 2D surface enclosing the current density to get the total power radiated from the excitation as follows:

$$\alpha_{sc} = 2\iint_{\Sigma}(\vec{S}\bullet\vec{r})\tilde{C}(\beta - n_i k_0\cos\theta)dS \tag{13}$$

$$\tilde{C}(\xi) \approx \frac{2\sigma^2 L_c}{1+L_c^2\xi^2} \tag{14}$$

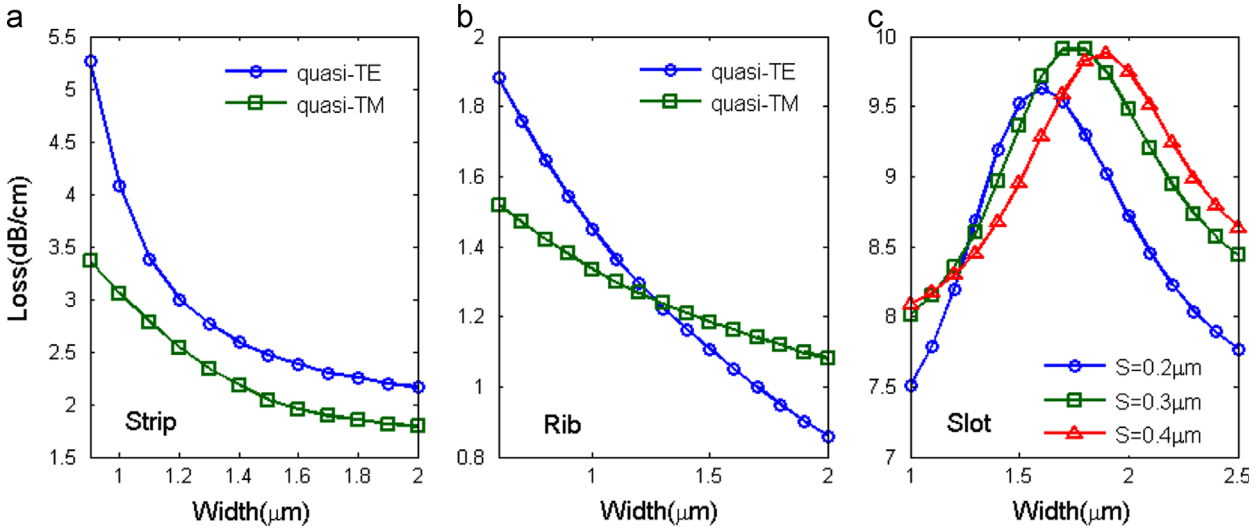

Fig. 8. Total propagation loss for three types of waveguides simulated using the volume–current method and beam-propagation method: (a) strip waveguide, $H=0.6$ μm; (b) rib waveguide, $H=0.6$ μm and $T=0.3$ μm and (c) slot waveguide, $H=0.6$ μm.

The integration is weighted by the array factor from the interference within the coherent length of the waveguide. $\vec{S}$ is the far-field power flow vector from the 3D simulation. $\tilde{C}(\xi)$ is the Fourier Transform of the roughness autocorrelation function. σ is the standard deviation of the surface roughness and L_c is the roughness coherent length. In order to estimate the values for $\sigma$and L_c for SOS waveguides, we use curve-fitting at two different wavelengths according to measured loss values from [14] and then we get the estimated values of $\sigma=13.4$ nm and $L_c=62.8$ nm. We also include the top and bottom waveguide roughness of $\sigma=2.6$ nmaccording to [32]. Meanwhile, we also considered the mode leakage loss by propagating the calculated mode for 1 cm using the beam propagation method.

The total propagation loss for all three types of waveguides is shown in Fig. 8. Strip waveguide shows a loss of 2–5 dB/cm for both quasi-TE and quasi-TM modes. The loss in the quasi-TM mode is generally lower than that in the quasi-TE mode for the same waveguide dimensions possibly due to the field enhancement at the sidewalls as shown in Fig. 3. Increasing waveguide width reduces the propagation loss by weakening the electrical field at the two sidewalls for both TE and TM modes. The propagation loss for the rib waveguide is much smaller than that for the strip waveguide, ranging from 0.9 dB/cm to 1.9 dB/cm. Quasi-TE mode is more sensitive to the waveguide width. We think that there are two reasons for this. First, the field enhancement at the sidewalls provides more momentum in the loss evolution. Second, the bell-shape mode distribution in quasi-TE mode favors lower loss when the waveguide is wide enough. Most notably, the slot waveguide suffers from considerably higher loss than the other two. The total loss can be as high as 7.5–10 dB/cm for the geometries under investigation. Just as the loss in strip and rib waveguides, the loss in the slot waveguide is also positively related with the EFR due to the fact that stronger evanescent field also means stronger electrical field at the sidewalls, which will be scattered. However, the propagation loss seems to be suppressed when the slot is narrow compared to wider slots. This is because narrower slot will trap the radiation better and result in smaller far-field radiations. Moreover, we found that the losses due to the sidewall roughness are more dominant and the scattering from top/bottom surfaces is negligibly small (<0.2 dB/cm for all cases).

All three types of waveguides are capable of achieving EFR as high as $>20\%$. However, the quasi-TE mode would generally offer a higher EFR and field–gas interaction. To achieve the same level of EFR, channel waveguide and rib waveguide have to be pushed to a smaller dimension than that of the slot waveguide. Among the three types of waveguides, rib waveguide shows the lowest loss, <2 dB/cm as estimated, and slot waveguide suffers from the largest propagation loss, as high as 10 dB/cm. The propagation loss is also strongly correlated with the EPR values in different waveguide geometries. Higher EPR values often come at the price of higher propagation loss. Since these intrinsic loss terms are static and the proposed sensing mechanism is based on the incremental loss due to the absorbing gas, we can always increase the incident power to compensate waveguide loss as will be shown in the next section, which presents the sensing of CO_2 gas in the atmosphere as a case study.

4. CO_2 sensing

Providing moderate EFR values, these waveguides can be incorporated to form evanescent field absorption gas sensors. As an example, we calculate the sensing resolution of CO_2 fluctuation in the atmosphere using parameters from commercial detectors and laser. The incident power of the input light source is set at 10 mW and its RIN is -139 dBc/Hz [33]. The base concentration c of CO_2 is chosen to be the latest atmospheric level of 396.8 ppm [34]. The absorption coefficient of CO_2 is 1214 L cm^{-1}/mol [35]. We first investigate the impact of EPR values by assuming a waveguide propagation loss of 4 dB/cm [13,14]. The total coupling loss is assumed to be -15 dB [36]. We investigate the system performance using three types of mid-IR detectors: InSb, HgCdTe and PbSe detectors. The former is a liquid nitrogen cooled photovoltaic detector and the latter two are room-temperature photoconductive detectors. As presented in Table 1, their operating parameters are adopted from commercial manufactures, e.g. Vigo and Hamamatsu [37,38].

Fig. 9 shows the sensitivity of the gas sensor for different EFR values and waveguide lengths. As we increase the length of waveguide employed in the sensor, the sensitivity first increases and then decreases after reaching the peak value. The increase is a result of longer interaction path. When the path length gets longer than the optimal value, however, the sensitivity begins to drop due to the over-attenuation of the signal, which can be alleviated by lowering the intrinsic loss. This poses a direct incentive for fabrication of low loss waveguides. As expected, high EFR gives rise to higher sensitivity. It is also noteworthy that the optimum

waveguide length for peak sensitivity is larger for higher EFR values.

Fig. 10 shows the gas sensing resolution for different waveguide lengths and EFR values using the three types of detectors. As the waveguide length increases from zero, the sensing resolution increases (Δc gets smaller) due to the increase in sensitivity. However, the resolution starts to drop as L increases further in HgCdTe and PbSe detectors. The reason for this is that thermal noise dominates in these room-temperature detectors and the lowering of sensitivity directly diminishes the resolution performance. This is, however, not the case in InSb detector. In the cooled photovoltaic detector, thermal noise is largely suppressed and shot noise dominates. The drop in sensitivity is compensated by the reduction of shot noise due to lower input power to the detector. Optimal detection resolution can be achieved in waveguides of about 1 cm. A sensing resolution of 2 ppm, 5 ppm and 50 ppm can be achieved in cooled InSb, room-temperature HgCdTe and room-temperature PbSe detectors respectively. The resolution performance is comparable to the state-of-art benchmarks for CO_2 sensors in the market: 3 ppm in [39] and 1 ppm in [40,41]. The speed of the sensor is limited by the mid-IR detector. By detecting the mid-IR signal indirectly using the same SOS platform and near-IR detectors as proposed in [16,17], real-time high-speed sensing is achievable. The resolution can even be boosted using quasi-phase-matching based amplification enhancement techniques in silicon waveguides [42,43].

Table 1
Detector parameters used in calculation.

	T (K)	λ_{op} (μm)	R	R_L (Ω)	I_d	NEP (W/Hz$^{1/2}$)
PbSe	300	4.0	3×10^3 [V/W]	0.3 M	N/A	8×10^{-11}
HgCdTe	293	4.0	3×10^3 [V/W]	1 K	N/A	3.1×10^{-12}
InSb	77	4.0	2.5 [A/W]	1 M	10 μA	5.5×10^{-13}

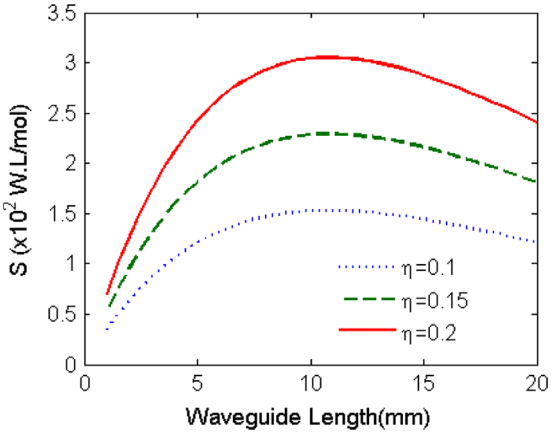

Fig. 9. Sensitivity, S, of the evanescent absorption gas sensor for different evanescent field ratios and waveguide lengths. An EFR of 0.2 provides about twice the sensitivity of that given by an EFR of 0.1.

We also studied the impact of different propagation losses and input powers on the detection resolution. Fig. 11 shows the calculated sensing resolution based on different propagation losses (4 dB/cm and 10 dB/cm) and input powers (10 mW and 50 mW) when they are detected by the same three types of detectors. As expected, the increase in propagation loss over-attenuated the signal and led to the degradation of the detection resolution when the waveguide was too long. However, as expected we can still compensate the loss by increasing the incident power at the input. As shown in Fig. 11, the sensing resolution for high loss waveguide can be restored, or even be boosted by increasing the input power from 10 mW to 50 mW for all three types of mid-IR detectors.

5. Summary

In summary, strip, rib and slot waveguides are designed for high evanescent field ratio to increase sensing resolution of the proposed evanescent field absorption gas sensor. Slot waveguide can provide the highest EFR ($>25\%$) in mid-IR with moderate waveguide dimension, but its fabrication is more challenging especially when slot width is small for high EFR. And its propagation loss is also much higher than

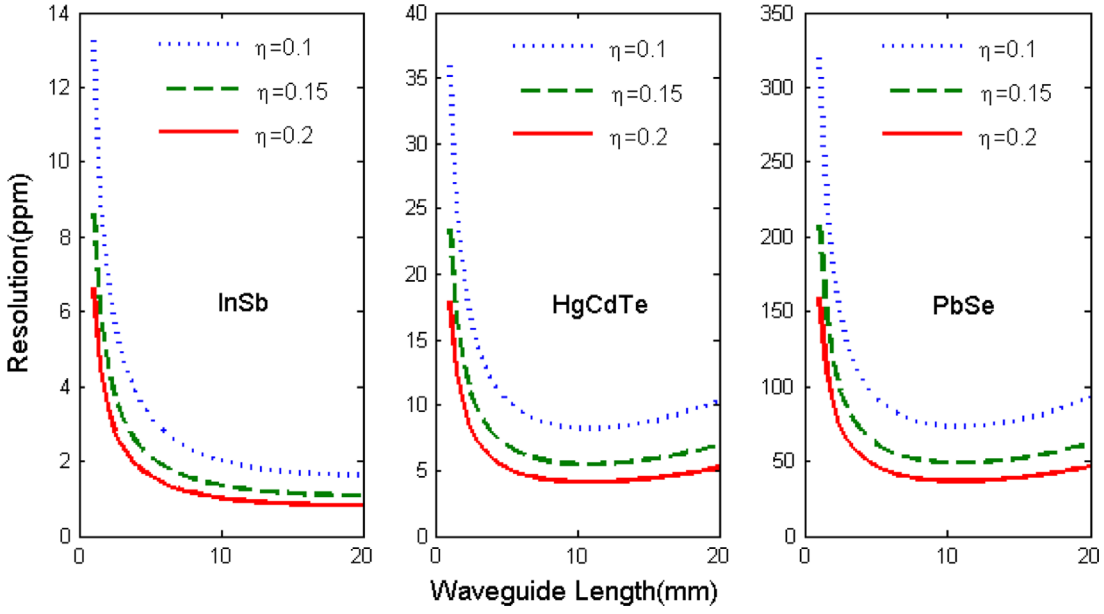

Fig. 10. Sensing resolution for different waveguide lengths with typical EFR values. Best sensing resolution of 2 ppm, 5 ppm and 50 ppm can be achieved in cooled InSb, room-temperature HgCdTe and room-temperature PbSe detectors respectively in ~1 cm waveguides.

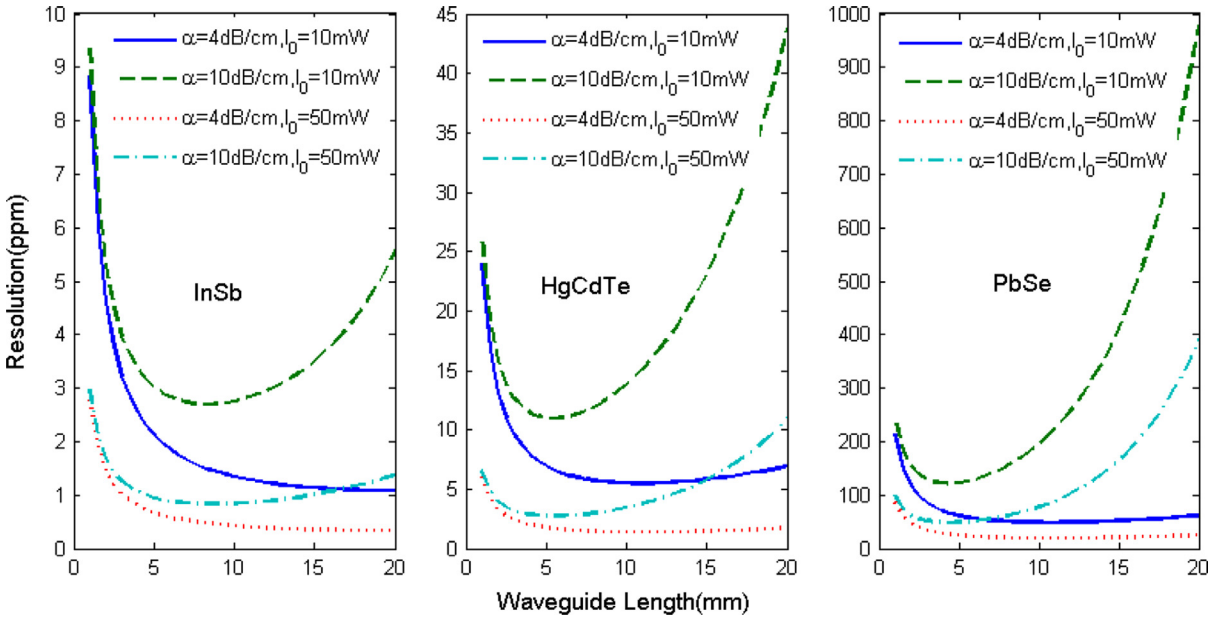

Fig. 11. Sensing resolution with different propagation losses and input powers; EPR was assumed to be 0.15 in all cases. Increase in waveguide loss degrades the sensing resolution performance, especially when the waveguide is long. However, higher input power can be utilized to compensate the propagation loss.

those of other two types, which makes higher input power necessary to achieve acceptable sensing resolution. Strip and rib waveguides can achieve similar EFR with smaller dimension. Moreover, rib waveguide can achieve propagation loss as low as <2 dB/cm, which also favors its application as an evanescent absorption sensor. As an example, we analyze the detection resolution for CO_2 in atmosphere based on the EFR values at the CO_2 absorption peak (4.23 μm). Our analysis shows that a resolution of 2 ppm, 5 ppm and 50 ppm can be achieved in cooled InSb, room-temperature HgCdTe and room-temperature PbSe detectors respectively in $\sim$1 cm waveguides with moderate input power. This resolution is adequate for many environmental applications.

Acknowledgment

This research was supported by DARPA Young Faculty Award, #66001-10-1-4036 and EU PIRG07-GA-2010-268370 grant. The authors want to thank Sam Crivello from Daylight Solution for valuable discussion. The authors would also like to thank the anonymous reviewers for their valuable comments and suggestions to improve the quality of the paper.

References

[1] D. Kohl, J. Phys. D: Appl. Phys. 34 (19) (2001) R125.
[2] K. Arshak, E. Moore, G.M. Lyons, J. Harris, S. Clifford, Sens. Rev. 24 (2) (2004) 181.
[3] J.T. Robinson, L. Chen, M. Lipson, Opt. Express 16 (6) (2008) 4296.
[4] N. Fabricius, G. Gauglitz, J. Ingenhoff, Sens. Actuators B: Chem. 7 (1–3) (1992) 672.
[5] Y. Huang, S. Kalyoncu, Q. Song, O. Boyraz, Silicon-on-sapphire waveguides design for mid-IR evanescent field absorption gas sensors, in: Proceedings of CLEO, JW2A.122, 2012.
[6] Michael B. Frish, Raji Shankar, Irfan Bulu, Ian Frank, Matthew C. Laderer, Richard T. Wainner, Mark G. Allen, Marko Lončar, Proc. SPIE 8631 (2013) 86310E.
[7] G. Stewart, W. Jin, B. Culshaw, Sens. Actuators B: Chem. 38 (1) (1997) 42.
[8] R. Siebert, J. Müller, Sens. Actuators A: Phys. 119 (1) (2005) 138.
[9] Yang Xia, Ciyuan Qiu, Xuezhi Zhang, Weilu Gao, Jie Shu, Qianfan Xu, Opt. Lett. 38 (2013) 1122.
[10] Pao Tai Lin, Vivek Singh, Yan Cai, Lionel C. Kimerling, Anu Agarwal, Opt. Lett. 38 (2013) 1031.
[11] R.A. Soref, S.J. Emelett, W.R. Buchwald, J. Opt. A: Pure Appl. Opt. 8 (2006) 840.
[12] E. Tien, Y. Huang, S. Gao, Q. Song, F. Qian, S. Kalyoncu, O. Boyraz, Opt. Express 18 (2010) 21981.
[13] T. Baehr-Jones, A. Spott, R. Ilic, A. Spott, B. Penkov, W. Asher, M. Hochberg, Opt. Express 18 (2010) 12127.
[14] F. Li, S. Jackson, C. Grillet, E. Magi, D. Hudson, S. Madden, Y. Moghe, C.O. Brien, A. Read, S. Duvall, P. Atanackovic, B. Eggleton, D. Moss, Opt. Express 19 (2011) 15212.
[15] Zhaolu Wang, Hongjun Liu, Nan Huang, Qibing Sun, Jin Wen, Xuefeng Li, Opt. Express 21 (2) (2013) 1840.
[16] Y. Huang, E.K. Tien, S. Gao, S.K. Kalyoncu, Q. Song, F. Qian, E. Adas, D. Yildirim, O. Boyraz, Appl. Phys. Lett. 99 (2011) 181122.
[17] X. Liu, B. Kuyken, G. Roelkens, R. Baets, R.M. Osgood Jr, W.M.J. Green, Nat. Photonics 6 (2012) 667.
[18] S. Zlatanovic, J.S. Park, S. Moro, J.M.C. Boggio, I.B. Divliansky, N. Alic, S. Mookherjea, S. Radic, Nat. Photonics 4 (2010) 561.
[19] B. Kuyken, X. Liu, R. Osgood, R. Baets, G. Roelkens, W. Green, Opt. Express 21 (2013) 5931.
[20] P.S. Wijewarnasuriya, Yuanping Chen, G. Brill, B. Zandi, N.K. Dhar, IEEE Trans. Electron Devices 57 (4) (2010) 782. (April).
[21] E. Ryckeboer, A. Gassenq, N. Hattasan, B. Kuyken, L. Cerutti, J. Rodriguez, E. Tournie, G. Roelkens, W. Bogaerts, R. Baets, Integrated spectrometer and integrated detectors on Silicon-on-Insulator for short-wave infrared applications, in: Proceedings of CLEO: Science and Innovations, OSA Technical Digest (online), Optical Society of America, 2012, Paper CTu1A.3.
[22] G.P. Agrawal, Fiber-Optic Communication Systemsthird edition, Wiley-Interscience, New York, 2002.
[23] S. Nudelman, Appl. Opt. 1 (1962) 627.
[24] P. Bhattacharya, Semiconductor Optoelectronic DevicesPrentice Hall, Englewood Cliffs, NJ, 1994.
[25] A. Densmore, D.X. Xu, P. Waldron, S. Janz, P. Cheben, J. Lapointe, E. Post, IEEE Photonics Technol. Lett. 18 (23) (2006) 2520.
[26] D.-X. Xu, W.N. Ye, A. Bogdanov, D. Dalacu, A. Delage, P. Cheben, S. Janz, B. Lamontagne, M.-J. Picard, Proc. SPIE 5730 (2005) 158.
[27] M. Kuznetsov, H. Haus, IEEE J. Quantum Electron.19 (10) (1983) 1505.
[28] T. Barwicz, H.A. Haus, J. Lightwave Technol. 23 (9) (2005) 2719.
[29] C. Ciminelli, V.M.N. Passaro, F. Dell'Olio, M.N. Armenise, J. Eur. Opt. Soc. (2009) 09015.
[30] C.G. Poulton, C. Koos, M. Fujii, A. Pfrang, T. Schimmel, J. Leuthold, IEEE J. Sel. Top. Quantum Electron. 12 (6) (2006) 1306.
[31] COMSOL Multiphysics 4.3, COMSOL Inc.. 2013.
[32] Silicon-on-sapphire data sheet, IQE Silicon Compounds Ltd., United Kingdom, May 2012, ⟨http://www.iqep.com/silicon/⟩.
[33] Daylight Solutions, Unicorn™ II Laser Specifications, San Diego, CA, USA, May 2012.
[34] NOAA Earth System Research Laboratory (May 2012). Retrived from ⟨http://www.esrl.noaa.gov/⟩.
[35] Harald Behrens, Nathalie Tamic, Francois Holtz, Am. Mineral. 89 (2004) 301.
[36] Z. Cheng, X. Chen, C.Y. Wong, K. Xu, C.K.Y. Fung, Y.M. Chen, H.K. Tsang, IEEE Photonics J. 4 (1) (2012) 104.
[37] Vigo System, IR Detectors Catalogue, Ozarow Mazowiecki, May 2012, Poland.
[38] Hamamatsu Photonics, Characteristics and Use of Infrared Detectors, Solid State Division, Hamamatsu Photonics K.K, Tokyo, Japan, 2004.

[39] Vernier Technology, CO_2 Gas Sensors, Beaverton, OR, USA, May 2013 ⟨http://www.vernier.com/products/sensors/co2-bta/⟩.
[40] CONTROS Systems & Solutions GmbH, HydroC Carbondioxide Sensor, Kiel, Germany, May 2013, ⟨http://www.contros.eu/products-hydroC-CO2-OG.html⟩.
[41] PASCO Scientific, PASPORT Carbon Dioxide Gas Sensor, Roseville, California, May 2013, ⟨http://www.pasco.com/⟩.
[42] Yuewang Huang, En-Kuang Tien, Shiming Gao, Salih K. Kalyoncu, Qi Song, FengQian, Ozdal Boyraz, Proc. SPIE (2011)81200F.
[43] J. Driscoll, N. Ophir, R. Grote, J. Dadap, N. Panoiu, K. Bergman, R. Osgood, Opt. Express 20 (2012) 9227.